PAPER

Check for updates

Exploring the heteroanionic 2D materials RhSeCl and RhTeCl as promising semiconductor materials†

Domenic Nowak, [ID] *[a] Erik Käppler,[a] Martin Knupfer, [ID] [a] Subakti Subakti, [ID] [a] Axel Lubk, [ID] [a,b] Dmitriy Efremov,[a] Bastian Rubrecht, [ID] [a,b] Alexey Popov, [ID] [a] Andreas Koitzsch, [ID] [a] Udo Steiner, [ID] [c] Bernd Büchner, [ID] [a,b] Martin Valldor, [ID] [d] Nico Gräßler [ID] *[a] and Silke Hampel [ID] *[a]

Heteroanionic materials show promising potential as 2D semiconductors due to their tunable band gaps, making them excellent candidates for photocatalytic water splitting applications. We conducted detailed theoretical and experimental analysis of two selected materials by synthesizing crystals through chemical vapor transport and investigating the impact of anion variation on crystal structure and properties. Using powder X-ray diffraction and convergent beam electron diffraction, we elucidated the non-centro-symmetric space groups of these compounds. Thermochemical studies revealed the influence of the crystal structure on the decomposition points of both compounds. Theoretical investigations predict that both materials are indirect bandgap semiconductors, which is confirmed by electron energy loss spectroscopy and photoluminescence studies.

1 Introduction

Two-dimensional (2D) materials have attracted the attention of researchers since the discovery of graphene by Novoselov and Geim in 2004, due to their unique properties and vast potential for various applications.[1] Recently, this material class has arisen as prospective photocatalysts for water splitting, benefiting from their advantageous characteristics such as extensive surface area and short migration paths for charge carriers, attributed to their low-dimensional structure.[2] The primary focus of advancing the optical properties of these compounds lies in diversifying the cations[3,4] or reducing the number of

[a]*Institute for Solid State Research, Leibniz-Institute for Solid State and Materials Research Dresden, Helmholtzstraße 20, D-01069 Dresden, Germany.*
E-mail: d.nowak@ifw-dresden.de, n.graessler@ifw-dresden.de,
s.hampel@ifw-dresden
[b]*Institute for Solid State and Materials Physics, Technical University Dresden, D-01062 Dresden, Germany*
[c]*Faculty of Agriculture Environment and Chemistry, University of Applied Sciences Dresden, D-01069 Dresden, Germany*
[d]*Department of Chemistry, University of Oslo, NO-0315 Oslo, Norway*
†Electronic supplementary information (ESI) available: SEM/EDX results; XRD measurements to investigate macroscopical long-term stability; additional image about the crystal structure; images and information regarding the DFT simulations of the optical properties; images and information regarding XPS; images and information regarding diffuse reflection measurements; full data of the thermochemical measurements; information and results regarding the decomposition of RhTeCl. See DOI: https://doi.org/10.1039/d4dt01487a

the stacked layers,[5,6] while exploration of the anions, especially through combining different types, is rarely explored. In this regard, heteroanionic materials (HAMs) have received increasing scientific focus in recent years.[7] This new class of materials allows for not only the pairing of anions from the same group on the periodic table, such as bichalcogenides,[8] but also the joining of anions from different groups like chalcohalides.[7] A primary aim within the latter class of compounds is the tailoring of material properties. Leveraging anions with dissimilar charges, ionic radii, and electronegativity enables a spectrum of properties in the resulting materials. Beyond using different types of anions, the crystal structure of the resulting compounds also significantly influences their characteristics. A key attribute of heteroanionic compound crystal structures is the varied cation coordination. Furthermore, how the coordinated polyhedra connect is also crucial for determining the arrangement and properties. Comparable polyhedral coordination and element quantities can result in different structural forms within a given family of mixed anionic materials.[9,10] Examinations of the relationship between crystal structure and physical properties of HAMs have to this point mainly focused on quaternary oxopnictides and bichalcogenides.[7–9,11] A thorough investigation of layered HAMs has been conducted solely in the bismuth chalcohalide family.[12–14] The results indicate that in such heteroleptic layered materials, the anions can adopt two arrangements: either evenly distributed on both sides of a single layer or in full layers of a single anion.

Materials with such rare crystal structures are called 2D Janus materials. In a previous publication, we described the crystal growth and structure of the novel 2D Janus material RhSeCl.[15] Here, we present the structure–property relationships of the 2D material RhTeCl[16] and the 2D Janus material RhSeCl. We conducted a comprehensive analysis employing various techniques, including thermochemical, XPS, CBED, EELS, and SQUID data, and found that the specific arrangement of anions in the structure affects the properties of the materials.

2 Results and discussion

2.1 Synthesis and morphology

For the synthesis of RhTeCl, we modified the method of Köhler *et al.*[16] using tellurium tetrachloride as a chlorine source because it is easier to dose and less dangerous than pure chlorine gas. The bulk crystals of RhTeCl, synthesized by chemical vapor transport (CVT), are black and lustrous with a typical layered structure. Similarly to RhSeCl crystals, RhTeCl shows a range of morphological variations, including sharp-edged, well-defined nanoplatelets and aggregated nanostructures (see Fig. S2†). EDX mapping confirmed the homogeneous distribution of constituent elements within a RhTeCl crystal, as illustrated in Fig. 1. The elemental analysis performed using EDX provides validation of the expected compositions within the measurement errors. Note that there appears to be a slight overestimation of the rhodium content for both chalcochlorides. This is possibly due to the overlapping of X-ray emission peaks of chlorine ($K_{\alpha12}$: 2.62 keV, $K_{\beta1}$: 2.82 keV) and rhodium ($L_{\alpha12}$: 2.69 keV, $L_{\beta1}$: 2.83 keV), as demonstrated in Fig. S3.†[17] The elemental analysis from an average of ten measurements indicates a composition close to $Rh_{35.3(8)} Te_{33.8(9)} Cl_{30.9(1)}$ as reflected in the ESI Table S1.†

X-ray diffraction data are in agreement well with a Le Bail refinement (see Fig. 2), suggesting that even the bulk samples are phase-pure RhTeCl. However, a Rietveld refinement was challenging due to a low data/parameter ratio and strong texture effects in the powder data. The raised background in the diffraction pattern at low 2θ angles could be explained, for example, by scattering of the X-ray radiation in the air or the measurement geometry itself. XRD measurements of samples
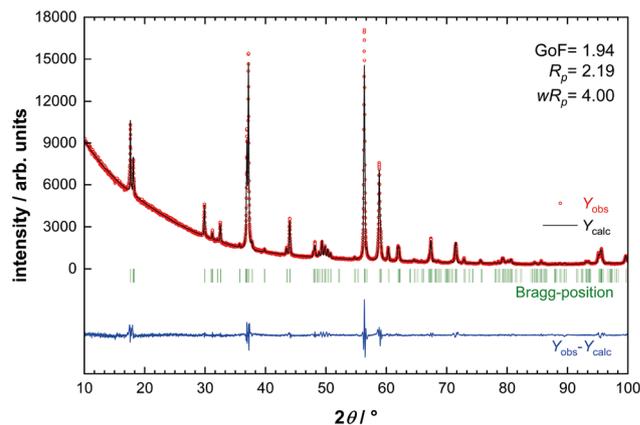

Fig. 2 Powder X-ray diffraction data of RhTeCl with superimposed LeBail refinement simulations and their corresponding differences. The measurement was carried out using a Cobalt K_α X-ray source (λ = 1.78896 Å).

from both chalcochlorides (see Fig. S3 and S4†) stored in normal atmospheric conditions over a longer period verified long-term stability. Accordingly, the behavior of the chalcochlorides is similar to the rhodium trihalides $RhCl_3$[18,19] and RhI_3,[5] which also show long-term environmental stability. The macroscopic long-term stability of the two chalcohalides accordingly opens up the possibility of using the two compounds for photocatalytic water splitting.[2,20]

2.2 Crystal structure

As described by Köhler *et al.*[16] RhTeCl crystallizes in a non-centrosymmetric monoclinic space group $C1m1$ with lattice constants a = 12.9881(2) Å, b = 3.6405(4) Å, c = 6.6528(1) Å and β = 118.76(2)° in a stacking order which can either be described as a distorted CdI_2 or an α-CrOOH structure type. In a previous publication,[15] we reported the crystal structure of the RhSeCl, which crystallizes in a hexagonal crystal structure (CdI_2 type) with the lattice constants a = 3.48760(1) Å and c = 11.5791(5) Å.

RhSeCl and RhTeCl have octahedra as the building units of their crystal structures, as shown in Fig. 3I. The anions in the octahedra exhibit a *facial* coordination in both materials. The distances between rhodium and chlorine, with approximately
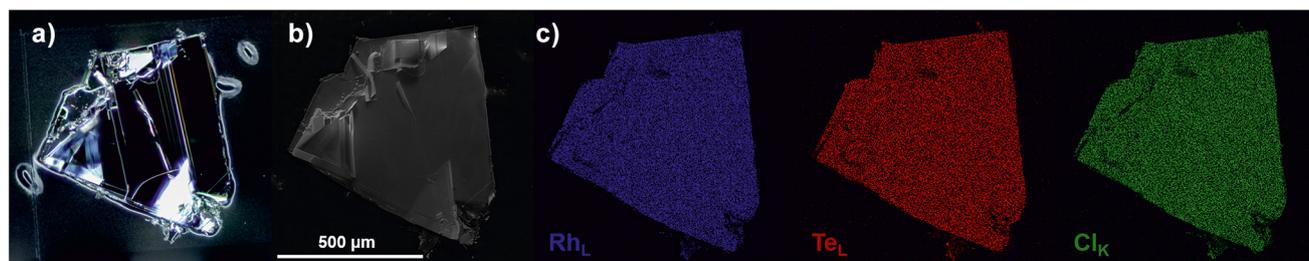

Fig. 1 (a) Light microscopy of a RhTeCl bulk crystal in dark field mode. (b) SEM image of the same crystal with some edge effects. (c) EDX spectroscopy mapping of the main elements of RhTeCl, showing a uniform distribution of the elements.
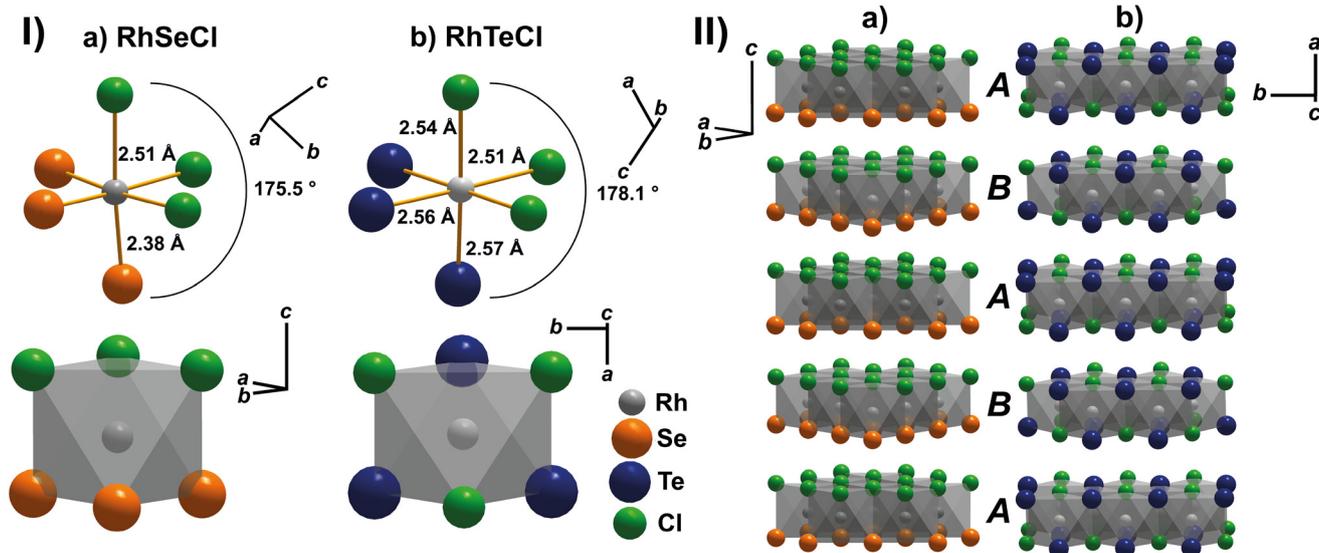
Fig. 3 I: Illustration of the coordination polyhedra, the atomic distances and the octahedral angle for RhSeCl (a) and RhTeCl (b). II: Section of the AB type layered crystal structure of the Janus material RhSeCl (a) and RhTeCl (b). RhSeCl is orientated in $b-c$ direction and RhTeCl in $b-a$ direction.[21]

2.51 Å, are equivalent in these compounds. Both HAMs have different rhodium chalcogen distances. In RhSeCl, the Rh–Se distances are 2.38 Å, which is 0.1 Å lower than those of Rh–Cl with 2.51 Å. On the other hand, the Rh–Te distances (2.56–2.57 Å) in RhTeCl are almost the same as those of Rh–Cl (2.51–2.54 Å). This difference in the interatomic distances between rhodium and the respective chalcogenide is due to the larger ionic radius of the tellurium (2.07 Å) compared to the selenium anion (1.84 Å).[22] Through the similarity of the halide and chalcogenide distances in RhTeCl, the distortion of the octahedral angle (178.1°) is less than in RhSeCl (175.5°). Due to the non-uniformity of the distances between either the Rh–Cl and the Rh–Te distances, RhTeCl exhibits fewer symmetry elements than RhSeCl, therefore the crystal space group is lower.

Fig. 3II demonstrates the AB stacking order of the 2D materials along their longest crystal axis for the c-axis of RhSeCl and the a-axis of RhTeCl. The arrangement of anions in the individual layers of rhodium chalcohalides differs. In RhSeCl, alternating layers of chlorine and selenium are present, which is consistent with the behavior of 2D Janus materials. On the other hand, in RhTeCl, the different anions are mixed in the layers. The difference in symmetry, and thus the space group, of the two compounds is related to the edge linkage of the coordination polyhedra, as illustrated in Fig. S6.† In RhSeCl, all edges are connected only through chalcogenide-chloride connections, which also exist in RhTeCl. However, chalcogenide and halide connections are more common in RhTeCl.

To determine the point and space group symmetries of RhTeCl and RhSeCl and confirm the Janus structure (*i.e.*, the absence of mirror symmetry with respect to the c-axis), we conducted convergent beam electron diffraction (CBED) measurements in a Transmission Electron Microscope (TEM) along different zone axes of RhSeCl (Fig. 4a) and RhTeCl (Fig. 4b). Here, the zero order Laue zone CBED patterns inherit the symmetry of the original point group (PG) restricted to the TEM lamella geometry prepared from the crystal.[23] By additionally analyzing systematically absent (forbidden) reflections as well as the presence of dynamical extinction lines[24,25] the whole space group (SG) symmetry could be unambiguously determined for the two compounds: In RhSeCl, a 6-fold rotational symmetry as well as two mirror plane symmetries are visible in the CBED pattern recorded along the [001] zone axis. In combination with the single mirror plane observed along [210] zone axis the PG is unambiguously fixed to 6*mm*. The additionally visible dynamical extinction lines in the indicated kinematically forbidden CBED disks (yellow arrows in Fig. 4a) are compatible with the presence of a 6_3 screw axis and a c glide plane, which together with the 6*mm* PG symmetry fixes the SG to the hexagonal *P*6_3*mc*. The only observable non-trivial CBED symmetry in RhTeCl (Fig. 4b) is a mirror plane visible in [101] orientation, which together with the forbidden reflections (*e.g.*, (11−1)along [112] orientation) fixes the SG to the monoclinic *Cm*.

Therefore, we could verify the non-centrosymmetricity of the described rhodium chalcohalides. Possible properties according to the Neumann principles for the Janus material, such as pyro- and piezoelectricity and non-linear optical behavior, were mentioned in an earlier publication.[15] Based on these principles, RhTeCl should show the same properties and additionally be optically active, *i.e.*, exhibit the rotation of polarization for light passing through this material.[26,27] This optical activity and the non-linear optical properties may be quenched due to the opaqueness of this crystal.

a) RhSeCl: SG: $P6_3mc$, PG: $6mm$
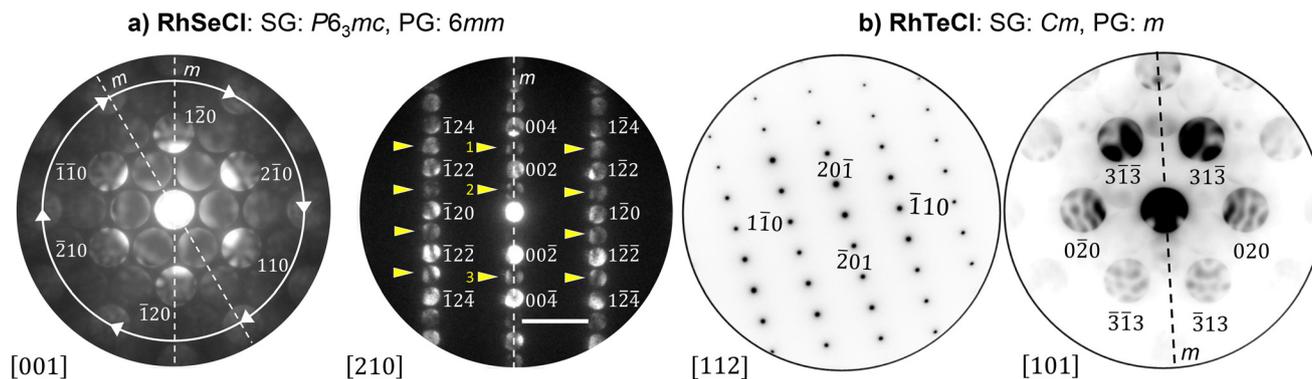
b) RhTeCl: SG: Cm, PG: m

Fig. 4 (a) CBED patterns including non-trivial symmetry elements and extinction lines (indicated by yellow arrows) of RhSeCl along [001] and [210] zone axis fixing the SG to $P6_3mc$. The scalebar corresponds to 4 nm^{-1}. (b) ED diffraction pattern along [112] including systematic absences (*e.g.,* (11−1)) and CBED pattern along [101] including the mirror plane symmetry fixing the SG of RhTeCl to Cm. We used an inverted grayscale for RhTeCl diffraction patterns to distinguish them from the RhSeCl results.

2.3 DFT simulations of the electronic structure

To gain insight into the electronic properties, we have performed electronic-structure calculations within the DFT theory. The full relativistic generalized gradient approximation (GGA) in the Perdew–Burke–Ernzerhof variant is used for the exchange–correlation potential implemented in the full potential local orbital band structure (FPLO) package.[28,29] For the Brillouin zone (BZ) integration, we used the tetrahedron method with a $12 \times 12 \times 12k$ mesh. We considered the nonmagnetic state. The band structure of RhSeCl and RhTeCl is shown in Fig. 5(I) and (II). The corresponding partial contributions of the electrons of the atoms to the density of states (PDOS) and the total density of states (DOS) are shown in Fig. 5(III) and (IV). The valence and conduction bands are dominated by the 4d electrons of Rh, the 3p electrons of Cl, and the 4p and 5p electrons of Se and Te, respectively. Both structures show semiconductor behavior with indirect gaps in the band structure of 1.17 eV and 0.68 eV in RhSeCl and RhTeCl, respectively. The optical gap of 1.48 eV in RhSeCl and 0.78 eV in RhTeCl can be seen in the loss functions (see ESI†). The trend of the calculated band-gap energies is comparable to that of the bismuth chalcohalides. Due to the growing number of electrons in the system, the band gap becomes smaller.[7,9,13] Furthermore, the results of our DFT calculations for the band gap of RhTeCl matched those of the *Materials Project* (Id. *mp-22945*) with 0.78 eV.[30,31] Qu *et al.*[32] likewise identified an indirect behavior of the band gap for bulk RhTeCl. However, like in MoS$_2$, there is a transition from an indirect to a direct band gap related to the number of atomic layers. Therefore calculations suggest that the band gap can be further tuned *via* defoliation.

2.4 Spectroscopic investigations

The relevant core levels of Rh 3d, Cl 2p and Se 3d are shown in detail in Fig. 6. For the overview XP spectrum of a single RhSeCl flake see Fig. S8 in ESI.† In addition to the expected signals for Rh, Se, and Cl, signals for oxygen and sodium were detected. In the Se 3d region, there is a broad peak marked with a star. This peak has a binding energy of 60 eV and corresponds to the presence of Na$_2$SeO$_4$ and/or SeO$_2$.[33]

The Janus material RhSeCl presents dissimilar surface layers on its opposing sides, either disposing Cl or Se. Therefore, the surface termination determines the relative intensities between Cl and Se in Fig. 6 due to the inherent surface sensitivity of photoemission spectroscopy. A pronounced surface dependency of the relative Cl/Se intensities is indeed evident. In addition, the Cl-terminated side is stable against the ambient atmosphere. The Se-terminated side exhibits elevated oxide components due to Selenium's inherent propensity to oxidize.[33] This kind of surface-dependent behavior of the respective anion intensities is analogous to the one found in the Janus material BiTeCl.[34]

For RhTeCl, an overview of the XP spectrum is displayed in Fig. S9.† Similar to the spectrum of RhSeCl, oxygen is also detectable as an additional element in RhTeCl. A detailed examination of the energy line of Te 3d is depicted in Fig. S10.† It is evident that there is a high-energy component, indicating oxide formation. Consequently, it seems that RhTeCl is more susceptible to surface oxidation than RhSeCl. This observation aligns with the behavior of other layered tellurium-containing compounds, such as WTe$_2$,[35,36] or MoTe$_2$,[37,38] which also oxidize relatively rapidly. The asymmetry of the Cl 2p line and the presence of aluminum energy lines in the overall spectrum can be attributed to the residues of the transport agent AlCl$_3$ on the surface.

The electronic excitation spectra of RhSeCl and RhTeCl were studied using electron energy-loss spectroscopy (EELS) in transmission mode. The corresponding data were taken at low momentum transfer, which is close to the optical limit, and they are depicted in Fig. 7. The data represent the so-called loss function and provide insight into the excitation onset and excitation features above. The excitation onset is a measure of the energy gap of the material, a fundamental physical parameter to characterize the electronic and transport behavior. The excitation onset has been determined by a linear extrapol-
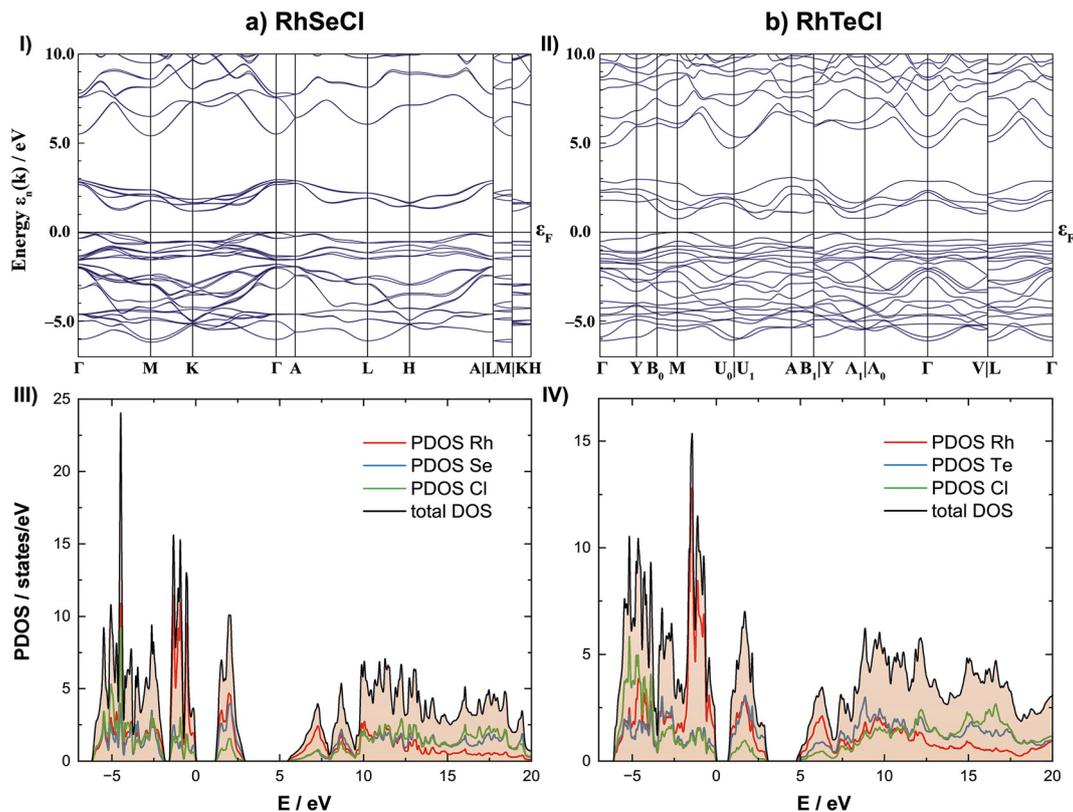
a) RhSeCl **b) RhTeCl**

Fig. 5 Electronic band structure (I and II) and atom-projected partial density of states (III and IV) for RhSeCl (a) and RhTeCl (b) calculated by PBE functional.
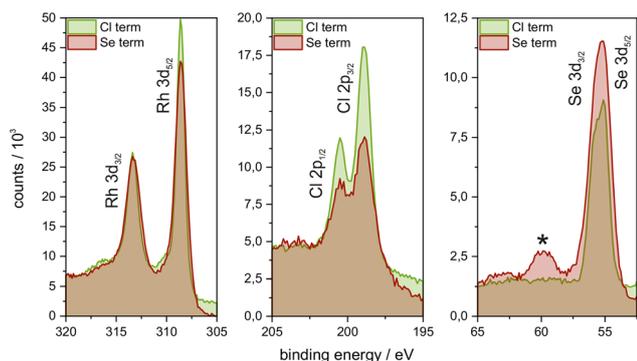

Fig. 6 XP spectra of shallow core levels comparing Cl- (green) and Se-terminated (red) RhSeCl. Each panel thus shows the respective spectra of the elements of RhSeCl. An additional * marked peak shows the presence of Na_2SeO_4 or SeO_2 on the surface of a selenium terminated sample.

ation of the data to zero. We observe an energy gap E_g of approximately 1.4 eV for RhSeCl and of about 0.7 eV for RhTeCl. The excitation spectra above the energy gap are rather featureless, which signals a broad and continuous-like joint density of states of the valence and conduction bands, respectively.

The photoluminescence of RhSeCl and RhTeCl has been measured on bulk crystals at various temperatures. The

results, as shown in (Fig. 8), indicate that substantial photoluminescence occurs at a temperature below 100 K for both chalcohalides. In the case of RhSeCl, we find a broad peak (from 1.2 to 1.6 eV) with a maximum signal at approximately 1.4 eV. A smaller feature at lower photon energies is likely an artifact of the detector, which loses the sensitivity in that energy range. RhTeCl displays two emission peaks, one at 0.75 eV and another in the energy range of 0.9 to 1.0 eV. The sharp shape of the feature at 0.75 eV is also likely affected by the sharp change of the detector response function below 0.75 eV, but the presence of the peak itself is unambiguous.

The extracted estimates of the band gap using electron energy loss and photoluminescence spectroscopy are largely consistent for both RhSeCl and RhTeCl and are close to the theoretically predicted values. Both compounds were thus confirmed to be semiconductors with a band gap in the near-infrared range: 885 nm for RhSeCl and 1771 nm for RhTeCl.[39] These observations verified that the band gap of the chalcohalide can be narrowed by selecting a chalcogenide anion with a lower electronegativity. In this case by exchanging the selenide with a telluride ion. However, the crystal lattice system and space group do not appear to have a direct influence on the band gap energy *per se*, but it is dependent on the structure type. This conclusion can be reached by comparing the experimental band gap energies of RhTeCl (0.7 eV) and BiTeCl (0.77 eV;[12] 0.8 eV (ref. 40)). Like RhSeCl, BiTeCl belongs to the
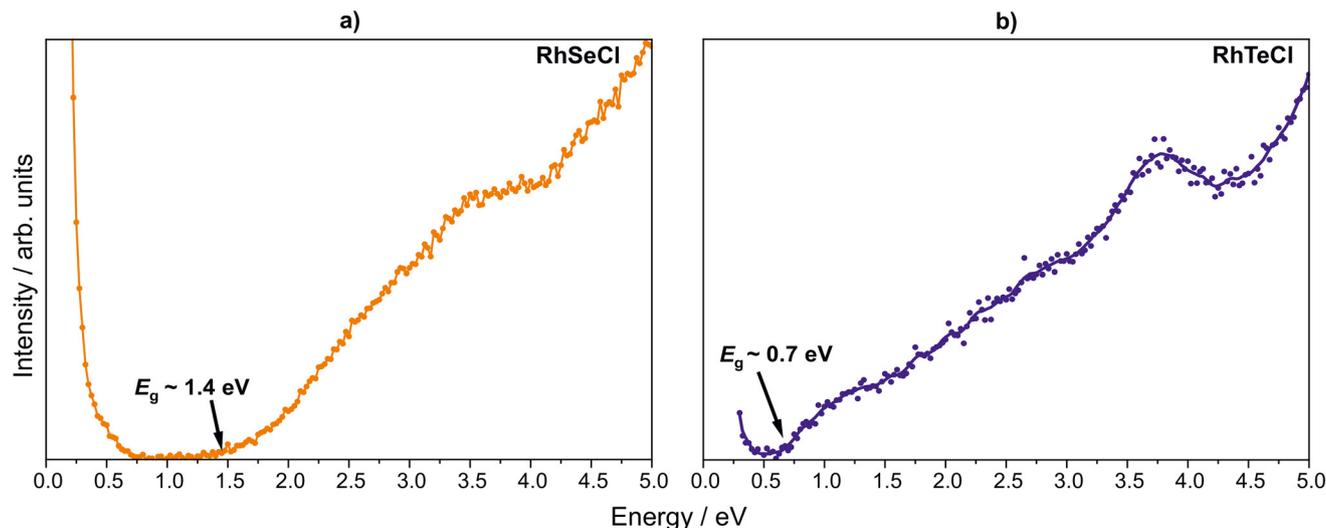
Fig. 7 Electronic excitation spectra of RhSeCl (a) and RhTeCl (b) as measured using EELS. The data have been taken with a small momentum transfer q, which corresponds to the optical limit ($q = 0.13$ Å^{-1} for both RhSeCl and RhTeCl).
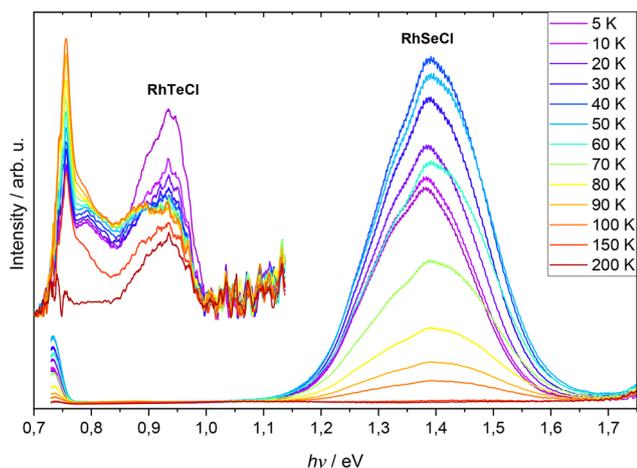

Fig. 8 Photo-luminescence spectra on bulk samples of RhSeCl and RhTeCl (insert), measured at various temperatures from 5 to 200 K and corrected for the detector response.

Cadium diiodide structure type (hexagonal, SG: $P6_3mc$), while RhTeCl (monoclinic, SG: Cm) exhibits a distorted variant of it.

2.5 Thermochemical investigation

RhSeCl exhibits thermal stability up to 700 °C as shown in the green TG-plot in Fig. 9. This is followed by a loss of mass, which occurs in two distinct phases. The first stage goes on till around 918 °C with a loss of around 13.4 weight percent and the second ends at 1000 °C with an additional 1.7 percent weight loss, indicating an almost complete evaporation of chlorine in this system. Through the tangent method, a decomposition point of 917 °C could be calculated, which is consistent with the large endothermic signal at 917.4 °C. Furthermore the two endothermic signals at 855.7 °C and 917.4 °C point towards two phase formations in the Rh–Se

system, where the latter correlates to the eutectic phase formation.[41,42] In contrast, the TG-plot for RhTeCl shows a significant mass loss of 32.13 percent. This mass loss corresponds to a total loss of chlorine as well as almost half of the tellurium content. The peak temperature of 760.6 °C of the first broad peak in the DSC plot is in agreement with the obtained decomposition point over the tangent method of the TG plot. Another large endothermic peak between 985.3 °C and 991.3 °C hints at the formation of an eutectic system of Rh and RhTe$_{2-x}$ and the peritecoidally forming of Rh$_3$Te$_2$ from Rh(Te) and RhTe$_{2-x}$.[43,44] The presence of elemental Rh and Rh$_3$Te$_2$ is revealed by subsequent PXRD analysis of the residue from the TG-DSC measurement see Fig. S10.†

2.6 Investigation of the magnetic behaviour

Fig. 10(a) shows the magnetic susceptibility of RhTeCl for the temperature range from 2 to 300 K. For temperatures above approximately 7 K, the curve exhibits diamagnetic behavior with a paramagnetic Curie-tail for the low-temperature regime. The measured susceptibility is well described by a modified Curie–Weiss behavior ($\chi = n \cdot C/(T - \Theta_{CW}) + \chi_0$). Here, n corresponds to the percentage of paramagnetic impurities, C is the Curie constant, Θ_{CW} the Curie–Weiss temperature, and χ_0 the temperature independent diamagnetic contribution. The fit yields a negligible paramagnetic fraction below 0.1% verifying the high purity of the grown single crystals. The obtained Curie constant and the corresponding effective moment of $\mu_{eff} = (6.5 \pm 0.1)\mu_B$ are in good agreement with the expected values for Rh^{2+}-ions. The fitted Curie–Weiss temperature is zero within the error bar of the experiment. The observed bulk signal of the sample corresponds to the diamagnetic χ_0 of about $-(5.76 \pm 0.25) \times 10^{-5}$ emu (mol Oe)$^{-1}$. Fig. 10(b) presents the magnetic moment as a function of the applied magnetic field. At temperatures of 1.8 K, we observe an increase of the
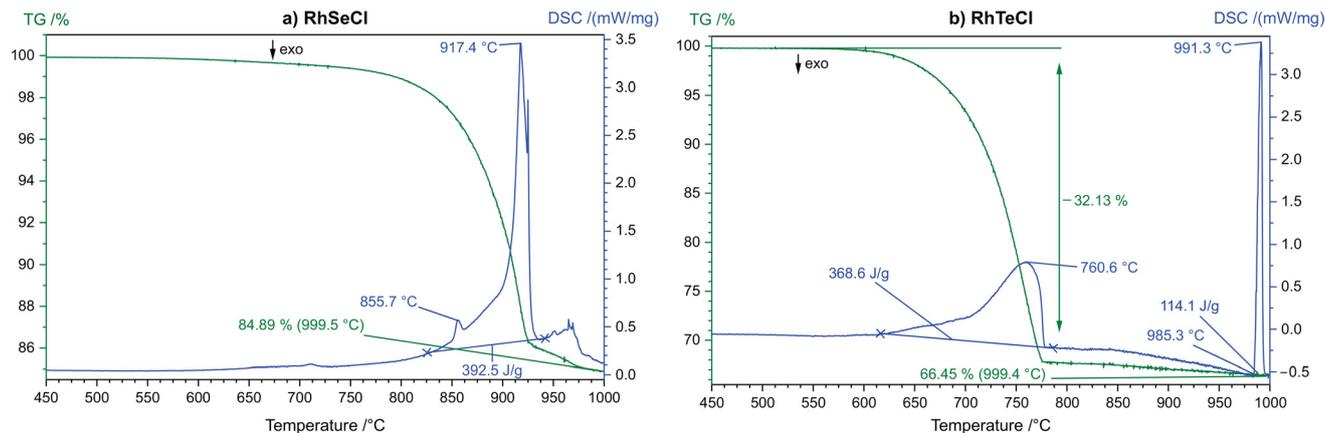
Fig. 9 TG-DSC data of RhSeCl (a) and RhTeCl (b) crystals starting from 450 °C up to 1000 °C, in green the TG and in blue the DSC measurement is plotted. The complete measured temperature range is shown in the ESI in Fig. S9.†
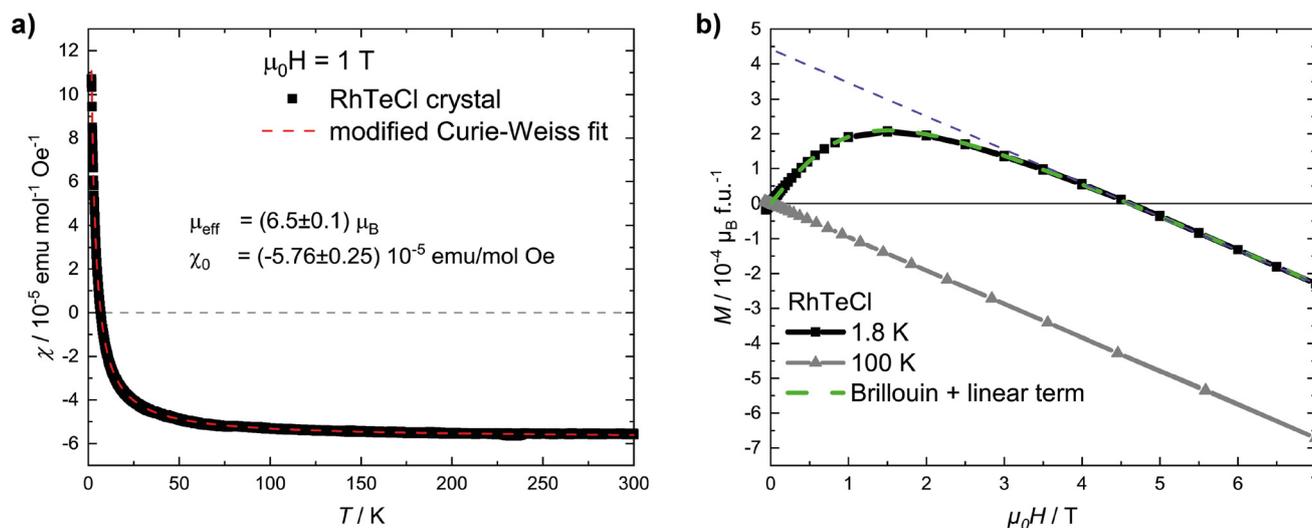

Fig. 10 (a) Magnetic susceptibility as a function of temperature of RhTeCl. The measurements were performed with an applied field of 1 T. The red dashed line corresponds to a modified Curie–Weiss fit; see text. (b) Magnetic moment as a function of the applied magnetic field at 1.8 and 100 K. The green dashed line corresponds to a scaled Brillouin fit ($n \cdot \mathcal{B}_J$) with an additional linear in-field contribution ($\chi_0 \cdot H$). The purple dashed line is a guide to the eye, corresponding to the saturation moment of the Brillouin-like contribution.

magnetic moment until 2 T followed by a downturn and a diamagnetic response. Moreover, above a magnetic field of 4 T, $M(H)$ follows a linear behavior. The observed behavior is well captured by a scaled Brillouin function and an additional linear term ($M(H) = n \cdot \mathcal{B}_J + \chi_0 \cdot H$). The obtained parameters agree well with the Curie–Weiss fit, corresponding to a small fraction ($n < 0.1\%$) of paramagnetic Rh^{2+}-ions, saturating at around 4–5 T at 4.4×10^{-4} μB per f.u. At higher temperatures ($T = 100$ K) a purely diamagnetic response is observed. Both linear regimes have the same linear slope of $\chi_0 = -(5.61 \pm 0.10) \times 10^{-5}$ emu (mol Oe)$^{-1}$, which is in good agreement with the Curie–Weiss fit. The observed mixture of *para-* and diamagnetic features are characteristic of samples with a diamagnetic main phase containing a small amount of uncorrelated paramagnetic impurities.

As for RhSeCl the octahedral crystal electric field (CEF) splits the 4d orbitals of the Rh^{3+} ion into three lower and two higher doubly degenerate energy levels, t_{2g} and e_g, respectively.[15] With all six valence electrons of the Rh^{3+} occupying the t_{2g} states, both spin and angular momentum of the rhodium ions are zero ($S = L = 0$). Compared to RhSeCl the diamagnetic response of the tellurium compound is stronger, which is expected due to the additional filled shell and the associated increased Larmor diamagnetism ($\chi_{\text{Larmor}} \propto -Z\langle r^2 \rangle$; Z: nuclear charge number and r: ionic radius[45]).

Due to the absence of a noteworthy magnetic moment in the magnetization measurements, an intrinsic localized magnetic moment residing on the Rh-ion can be ruled out, thus proving that Rh^{3+} is, for both compounds, the only existing oxidation state of the cation.
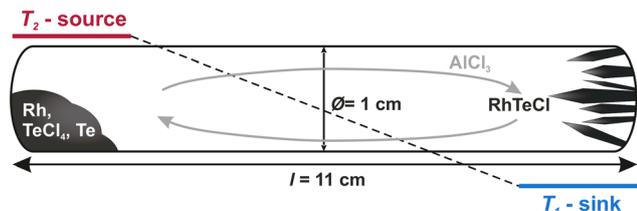
Fig. 11 Schematic of the growth configuration for the performed experiments. One-chamber ampoules (l = 11 cm, Θ = 1 cm) were used, with the starting material positioned on the source side and the crystals deposited on the sink side.

3 Conclusion

In this work we investigated the structure–property relationships in the ternary transition metal chalcohalides RhSeCl and RhTeCl using a variety of characterization methods. Through X-ray and converged electron beam diffraction, we demonstrated the non-centrosymmetricity of RhSeCl and RhTeCl, thus verifying the initially published crystal structures. While RhTeCl has a crystal structure that corresponds to the distorted CdI_2 structure type, the compound RhSeCl is a Janus material, which shows a clear separation of the anions. The different arrangement of the anions in the crystal structure of these two materials results in very distinct properties. The Janus character of RhSeCl was confirmed *via* XPS, as there is a site dependency of the oxidation behavior as well as the intensity of the anionic species. Furthermore, the used spectroscopic characterization methods and the theoretical calculations agree in their core findings, that both materials are semiconductors with a band gap in the near-infrared wavelength regime. The observed reduction in the band gap from RhSeCl to RhTeCl can be explained using a common theory for heteroanionic materials and compared with the bismuthchalcochloride system. Through the results of the thermochemical characterization, we can conclude, that the Janus material is more stable against decomposition than the structurally related RhTeCl. SQUID measurements showed diamagnetic behavior in both investigated compounds, implying that the only cationic species in these materials is Rh^{3+}. Further physical investigations are warranted to validate the expected piezoelectric and pyroelectric properties, consistent with Neumann principles, expected in both compounds.

4 Materials and methods

4.1 Synthesis of the rhodiumchalcohalides

$RhCl_3$ (rhodium(III) chloride, 99%, Abcr, lot 1251061) Rh (rhodium, 99.95%, Sigma-Aldrich, lot MKCR3908), Se (selenium, 99.999%, AlfaAesar, lot S17G004), Te (tellurium, 99.999%, AlfaAesar, lot 61600593), $TeCl_4$ (tellurium(IV) chloride, 99.9%, AlfaAesar, lot Q09B057) and $AlCl_3$ (aluminium(III) chloride, 99.999%, AlfaAesar, lot M12C021) were used for the synthesis. All chemicals were handled inside an *MBraun MB-*

200B ECO Glovebox at <1 ppm O_2 and <1 ppm H_2O. The procedure to synthesize RhSeCl is described in our previous publication.[15] For the synthesis of RhTeCl a stoichiometric ratio of 4 : 3 : 1 of rhodium, tellurium, and tellurium(IV)-chloride with a slight addition of aluminum(III)-chloride was chosen for the crystal growth *via* chemical vapor transport (CVT). The chemicals were mixed in an agate mortar and then transferred to a fused silica (imasil PN, qsil, max. 45 ppm OH content) single chamber ampoule. The ampoule was sealed with a hydrogen–oxygen torch under vacuum at 10^{-3} Pa.

The CVT was carried out with a temperature gradient of $\Delta T = 200$ K ($T_1 = 700$ °C, $T_2 = 900$ °C) and an heating rate of 2.5 K min^{-1}, see Fig. 11. After four days, the ampoule was allowed to naturally cool down to room temperature and black, shiny crystals of RhTeCl were visible in the sink area. After opening the ampoules, ethanol was added to the sink side and transferred to an ultrasonic bath for 2 minutes to detatch the crystals from the glass wall.

4.2 Microscopical investigation

The crystals grown *via* CVT were investigated through light microscopy with the AXIO Imager.A1M (Fa. Zeiss, Germany). Therefore, we used the dark field image mode. SEM images were obtained using a Nova NanoSEM (Fa. FEI Company, USA) with a through-the-lens detector. The chosen acceleration voltage varied between 15 keV. For the EDX analysis and mapping, we used a QUANTA 200/400 (Fa. AMETEX) with an acceleration voltage of 25 keV integrated into the SEM.

4.3 Structural characterization

Powder X-ray diffraction (PXRD) measurements were performed using a STADI P (STOE, Germany) device (Ge (111) primary beam monochromator, Mythen 1K detector, 0.015° step size) in transmission geometry with a Co source (λ = 1.78896 Å). For the Le Bail refinement, the Jana2020 program package[46] was used. After thermochemical analysis, the samples were analyzed using an XRD 3003TT diffractometer from GE Inspection Technologies with a Cu source (λ = 1.5406 Å). Measurements were taken in Bragg–Brentano geometry with a Ketek AXAS-M energy-dispersive SSD detector.

The CBED patterns have been recorded at a FEI Titan^3 TEM using 300 kV acceleration voltage. Note that small misorientations as well as thickness variations lead to small symmetry violations, which can be neglected in the analysis.

4.4 Spectroscopic investigation

X-ray photoelectron spectroscopy (XPS) was carried out using a PHI 5600 spectrometer from Physical Electronics. Monochromatized AlKα radiation with a power of 250 W was used. The hemispherical analyzer was set to a pass energy of 93.9 eV for the survey scan and 29.35 eV for the fine scans of the core levels. The spot size was 0.4 mm. The samples were handled exclusively in a glovebox to prevent air contact and surface contamination before being transferred to a transfer chamber for examination. The spectra were referenced to the C 1s peak at 284.8 eV to correct charging effects during the

measurements. Electron energy loss spectroscopy (EELS) was performed using a home-built spectrometer with a primary electron energy of 172 keV.[47,48] The energy resolution was set to 85 meV, and the momentum resolution to 0.035 Å^{-1}. All measurements have been carried out at room temperature. The polycrystalline RhSeCl sample (1–2 mg) was dispersed in a few drops of ethanol and exfoliated *via* ultrasonification. A few drops of the fresh dispersion were then pipetted onto a copper grid with lacey-carbon coating (Science Service GmbH, 200 mesh) to collect a sufficient amount of the dispersed material. The grid was then dried under a vacuum. For RhTeCl, a 100 nm thick film has been prepared *via* exfoliation from a single crystal and subsequently put onto a copper grid. Photoluminescence measurements were performed in back-scattering geometry using a microscope of home design and laser excitation at 488 nm (Omicron PhoxX diode laser). PL detection was done using Kymera 328i spectrograph (Andor) and iDus 1.7 μm InGaAs camera (Andor), calibrated *versus* black body radiation. The temperature of the sample was controlled with Janis ST-500 microscopy cryostat.

4.5 Simultaneous thermal analysis

DSC, coupled with TG was performed with a NETZSCH STA 449C (NETZSCH-Gerätebau GmbH). Pt–Rh-crucibles were loaded with about 20 mg material (powder for RhSeCl and finely ground crystals for RhTeCl) and covered with a lid, applying a heating rate of 10 K min^{-1} from 20 °C to 1000 °C. A N_2 (99.999, <2 ppm O_2) gas flow of 50 ml min^{-1} was applied. Before the analysis, the DSC signal was calibrated using measurements of transition enthalpies of standard substances (KNO_3, $RbNO_3$, $KClO_4$, Ag_2SO_4, $CsCl$, K_2CrO_4, $BaCO_3$).

4.6 Magnetic measurements

Magnetic measurements of RhTeCl crystals were performed in a VSM-SQUID magnetometer (MPMS, Quantum Design). The variation of magnetization with temperature was recorded in field-cooled (FC) mode in the range from 300 K to 2 K and an applied field of 1 T.

Author contributions

D. N.: Conceptualization, methodology, investigation, writing – original draft, writing – review & editing, visualization, funding acquisition; E. K.: methodology, writing – review & editing; M. K., S. S., A. L., B. R., A. P., A. K. and U. S.: investigation, writing – original draft, writing – review & editing; D. E.: formal analysis, writing – original draft, writing – review & editing, funding acquisition; B. B.: resources, writing – review & editing, supervision, funding acquisition; M. V.: writing – original draft, writing – review & editing, supervision, funding acquisition; N. G.: writing – original draft, writing – review & editing, supervision; S. H.: writing – original draft, writing – review & editing, supervision, project administration, funding acquisition.

Data availability

The data supporting this article have been included as part of the ESI.†

Conflicts of interest

The authors declare that they have no known competing financial interests or personal relationships that could have appeared to influence the work reported in this paper.

Acknowledgements

References

1 K. S. Novoselov, A. K. Geim, S. V. Morozov, D. Jiang, Y. Zhang, S. V. Dubonos, I. V. Grigorieva and A. A. Firsov, Electric Field Effect in Atomically Thin Carbon Films, *Science*, 2004, **306**, 666–669.

2 Y. Ying, Z. Lin and H. Huang, "Edge/Basal Plane Half-Reaction Separation" Mechanism of Two-Dimensional Materials for Photocatalytic Water Splitting, *ACS Energy Lett.*, 2023, **8**, 1416–1423.

3 M. Zhang, J. Wu, Y. Zhu, D. O. Dumcenco, J. Hong, N. Mao, S. Deng, Y. Chen, Y. Yang, C. Jin, S. H. Chaki, Y.-S. Huang, J. Zhang and L. Xie, Two-Dimensional Molybdenum Tungsten Diselenide Alloys: Photoluminescence, Raman Scattering, and Electrical Transport, *ACS Nano*, 2014, **8**, 7130–7137.

4 Y. Sun, K. Fujisawa, Z. Lin, Y. Lei, J. S. Mondschein, M. Terrones and R. E. Schaak, Low-Temperature Solution Synthesis of Transition Metal Dichalcogenide Alloys with Tunable Optical Properties, *J. Am. Chem. Soc.*, 2017, **139**, 11096–11105.

5 F. Wang, Z. Zhang, Y. Zhang, A. Nie, W. Zhao, D. Wang, F. Huang and T. Zhai, Honeycomb RhI 3 Flakes with High

Environmental Stability for Optoelectronics, *Adv. Mater.*, 2020, **32**, 202001979.

6 A. Chaves, J. G. Azadani, H. Alsalman, D. R. da Costa, R. Frisenda, A. J. Chaves, S. H. Song, Y. D. Kim, D. He, J. Zhou, A. Castellanos-Gomez, F. M. Peeters, Z. Liu, C. L. Hinkle, S.-H. Oh, P. D. Ye, S. J. Koester, Y. H. Lee, P. Avouris, X. Wang and T. Low, Bandgap engineering of two-dimensional semiconductor materials, *npj 2D Mater. Appl.*, 2020, **4**, 29.

7 H. Kageyama, K. Hayashi, K. Maeda, J. P. Attfield, Z. Hiroi, J. M. Rondinelli and K. R. Poeppelmeier, Expanding frontiers in materials chemistry and physics with multiple anions, *Nat. Commun.*, 2018, **9**, 772.

8 M. Valldor, Anion Ordering in Bichalcogenides, *Inorganics*, 2016, **4**, 23.

9 J. K. Harada, N. Charles, K. R. Poeppelmeier and J. M. Rondinelli, Heteroanionic Materials by Design: Progress Toward Targeted Properties, *Adv. Mater.*, 2019, **31**, 1–26.

10 N. Charles, R. J. Saballos and J. M. Rondinelli, Structural Diversity from Anion Order in Heteroanionic Materials, *Chem. Mater.*, 2018, **30**, 3528–3537.

11 G. Pilania, A. Ghosh, S. T. Hartman, R. Mishra, C. R. Stanek and B. P. Uberuaga, Anion order in oxysulfide perovskites: origins and implications, *npj Comput. Mater.*, 2020, **6**, 71.

12 A. Akrap, J. Teyssier, A. Magrez, P. Bugnon, H. Berger, A. B. Kuzmenko and D. Van Der Marel, Optical properties of BiTeBr and BiTeCl, *Phys. Rev. B: Condens. Matter Mater. Phys.*, 2014, **90**, 1–6.

13 Z. Ran, X. Wang, Y. Li, D. Yang, X.-G. Zhao, K. Biswas, D. J. Singh and L. Zhang, Bismuth and antimony-based oxyhalides and chalcohalides as potential optoelectronic materials, *npj Comput. Mater.*, 2018, **4**, 14.

14 S. Zhou, J. Long and W. Huang, Theoretical prediction of the fundamental properties of ternary bismuth tellurohalides, *Mater. Sci. Semicond. Process.*, 2014, **27**, 605–610.

15 D. Nowak, M. Valldor, B. Rubrecht, S. Froeschke, S. Eltoukhy, B. Büchner, S. Hampel and N. Gräßler, Crystal growth of the 2D Janus rhodium chalcohalide RhSeCl, *Inorg. Chem. Front.*, 2023, **10**, 2911–2916.

16 J. Köhler and W. Urland, RhTeCl – das erste Chalkogenidhalogenid eines Platinmetalls mit Schichtstruktur, *Z. Anorg. Allg. Chem.*, 1997, **623**, 583–586.

17 J. A. Bearden, X-Ray Wavelengths, *Rev. Mod. Phys.*, 1967, **39**, 78–124.

18 C. W. Jang, J. M. Kim, J. H. Kim, D. H. Shin, S. Kim and S.-H. Choi, Degradation reduction and stability enhancement of p-type graphene by RhCl3 doping, *J. Alloys Compd.*, 2015, **621**, 1–6.

19 S. Froeschke, K.-G. Schroth, U. Steiner, A. Popov, S. Schiemenz, D. Wolf, L. Giebeler, N. Gräßler, B. Büchner, P. Schmidt and S. Hampel, Understanding the chemistry of 2D rhodium trihalide solid solutions: tuning of optical properties and nanocrystal deposition, *2D Mater.*, 2023, **10**, 035011.

20 Y. Ying, K. Fan, S. Zhu, X. Luo and H. Huang, Theoretical Investigation of Monolayer RhTeCl Semiconductors as Photocatalysts for Water Splitting, *J. Phys. Chem. C*, 2020, **124**, 639–646.

21 H. Putz and K. Brandenburg GbR, *Diamond – Crystal and Molecular Structure Visualization*, 2022.

22 R. D. Shannon, Revised effective ionic radii and systematic studies of interatomic distances in halides and chalcogenides, *Acta Crystallogr., Sect. A: Cryst. Phys., Diffr., Theor. Gen. Crystallogr.*, 1976, **32**, 751–767.

23 B. F. Buxton, J. A. Eades, J. W. Steeds and G. M. Rackham, The symmetry of electron diffraction zone axis patterns, *Philos. Trans. R. Soc., A*, 1976, **281**, 171–194.

24 J. Gjønnes and A. F. Moodie, Extinction conditions in the dynamic theory of electron diffraction, *Acta Crystallogr.*, 1965, **19**, 65–67.

25 M. Tanaka, *International Tables for Crystallography*, International Union of Crystallography, Chester, England, 3rd edn, 2010, vol. B, pp. 307–356.

26 T. Hahn, H. Klapper, U. Müller and M. I. Aroyo, *International Tables for Crystallography*, International Union of Crystallography, 2016, vol. A, pp. 720–776.

27 W. Borchardt-Ott, *Crystallography*, Springer Berlin Heidelberg, Berlin, Heidelberg, 2012.

28 *FPLO*, https://www.fplo.de/.

29 K. Koepernik and H. Eschrig, Full-Potential Nonorthogonal Local-Orbital Minimum-Basis Band-Structure Scheme, *Phys. Rev. B: Condens. Matter Mater. Phys.*, 1999, **59**, 1743–1757.

30 A. Jain, S. P. Ong, G. Hautier, W. Chen, W. D. Richards, S. Dacek, S. Cholia, D. Gunter, D. Skinner, G. Ceder and K. A. Persson, Commentary: The Materials Project: A materials genome approach to accelerating materials innovation, *APL Mater.*, 2013, **1**, 011002.

31 J. M. Munro, K. Latimer, M. K. Horton, S. Dwaraknath and K. A. Persson, An improved symmetry-based approach to reciprocal space path selection in band structure calculations, *npj Comput. Mater.*, 2020, **6**, 112.

32 H. Qu, S. Guo, W. Zhou, B. Cai, S. Zhang, Y. Huang, Z. Li, X. Chen and H. Zeng, Electronic structure and transport properties of 2D RhTeCl: a NEGF-DFT study, *Nanoscale*, 2019, **11**, 20461–20466.

33 U. Weser, G. Sokolowski and W. Pilz, Reaction of selenite with biochemically active thiols: An X-ray photoelectron spectroscopic study, *J. Electron Spectrosc. Relat. Phenom.*, 1977, **10**, 429–439.

34 G. Landolt, S. V. Eremeev, O. E. Tereshchenko, S. Muff, B. Slomski, K. A. Kokh, M. Kobayashi, T. Schmitt, V. N. Strocov, J. Osterwalder, E. V. Chulkov and J. Hugo Dil, Bulk and surface Rashba splitting in single termination BiTeCl, *New J. Phys.*, 2013, **15**, 085022.

35 C.-H. Lee, E. C. Silva, L. Calderin, M. A. T. Nguyen, M. J. Hollander, B. Bersch, T. E. Mallouk and J. A. Robinson, Tungsten Ditelluride: a layered semimetal, *Sci. Rep.*, 2015, **5**, 10013.

36 A. Chen, H. Li, R. Huang, Y. Zhao, T. Liu, Z. Li, L. Wang, F. Chen, W. Ren, S. Lu, B. Yang, Z. Huang, S. Ding and

F.-S. Li, Observation of band bending in WTe2 after surface oxidation, *Surf. Sci.*, 2022, **716**, 121956.

37 J. Bernède, C. Amory, L. Assmann and M. Spiesser, X-ray photoelectron spectroscopy study of MoTe2 single crystals and thin films, *Appl. Surf. Sci.*, 2003, **219**, 238–248.

38 T. T. Pham, R. Castelino, A. Felten and R. Sporken, Study of surface oxidation and recovery of clean MoTe2 films, *Surf. Interfaces*, 2022, **28**, 101681.

39 T. J. Bruno and P. D. Svoronos, *CRC handbook of fundamental spectroscopic correlation charts*, CRC Press, 2005, pp. 1–226.

40 Y. L. Chen, M. Kanou, Z. K. Liu, H. J. Zhang, J. A. Sobota, D. Leuenberger, S. K. Mo, B. Zhou, S.-L. Yang, P. S. Kirchmann, D. H. Lu, R. G. Moore, Z. Hussain, Z. X. Shen, X. L. Qi and T. Sasagawa, Discovery of a single topological Dirac fermion in the strong inversion asymmetric compound BiTeCl, *Nat. Phys.*, 2013, **9**, 704–708.

41 B. Predel, *Phase Equilibria, Crystallographic and Thermodynamic Data of Binary Alloys*, Springer-Verlag, Berlin/Heidelberg, 1998, pp. 1–2.

42 T. E. Rummery and R. D. Heyding, The rhodium/selenium system, *Can. J. Chem.*, 1967, **45**, 131–137.

43 F. Predel, *Phase Equilibria, Crystallographic and Thermodynamic Data of Binary Alloys*, Springer Berlin Heidelberg, Berlin, Heidelberg, 2016, pp. 215–216.

44 Z. Ding, H. Kleykamp and F. Thümmler, The constitution of the rhodium-tellurium system, *J. Nucl. Mater.*, 1990, **171**, 134–138.

45 N. W. Ashcroft and N. D. Mermin, *Solid State Physics*, Holt-Saunders, 1976.

46 V. Petříček, L. Palatinus, J. Plášil and M. Dušek, Jana2020 – a new version of the crystallographic computing system Jana, *Z. Kristallogr. – Cryst. Mater.*, 2023, **238**, 271–282.

47 J. Fink, Recent developments in energy-loss spectroscopy, *Adv. Electron. Electron Phys.*, 1989, **75**, 121–232.

48 F. Roth, A. König, J. Fink, B. Büchner and M. Knupfer, Electron energy-loss spectroscopy: A versatile tool for the investigations of plasmonic excitations, *J. Electron Spectrosc. Relat. Phenom.*, 2014, **195**, 85–95.